Redox-active Chiroptical Switching in Mono- and Bis-Iron-Ethynyl-Carbo[6]Helicenes Studied by Electronic and Vibrational Circular Dichroism and Resonance Raman Optical Activity

Chengshuo Shen, Monika Srebro-Hooper, Florian Krausbeck, Thomas Weymuth, Juan López Navarrete, Francisco Ramirez, Belen Nieto-Ortega, Juan Casado, Markus Reiher, Jochen Autschbach, et al.

Redox-active Chiroptical Switching in Mono- and Bis-Iron-Ethynyl-Carbo[6]Helicenes Studied by Electronic and Vibrational Circular Dichroism and Resonance Raman Optical Activity

Chengshuo Shen,[a] Monika Srebro-Hooper,[b] Thomas Weymuth,[c] Florian Krausbeck,[c] Juan T. López Navarrete,[d] Francisco J. Ramírez,[d] Belén Nieto-Ortega,[d] Juan Casado,[d] Markus Reiher,[c] Jochen Autschbach,*[e] and Jeanne Crassous*[a]

Dedication ((optional))

Abstract: Introducing one or two alkynyl-iron moieties onto a carbo[6]helicene results in organometallic helicenes (**2a**,**b**) displaying strong chiroptical activity combined with efficient redox-triggered switching. The neutral and oxidized forms have been studied in detail by electronic and vibrational circular dichroism (ECD, VCD) as well as by Raman optical activity (ROA) spectroscopies. The experimental results were analyzed and spectra were assigned with the help of first-principles calculations. In particular, a recently developed method for ROA calculations under resonance conditions has been used to study the intricate resonance effects on the ROA spectra of mono-iron-ethynyl-helicene **2a**.

Introduction

Helicenes are a unique class of non-planar, polycyclic aromatic compounds whose helical backbone, formed by a variable number of *ortho*-fused benzene or other aromatic rings, renders them chiral despite the absence of a chiral center. The intrinsic chirality along with the extended π-conjugation in these systems explain some of their most important physico-chemical properties, including their large-magnitude chiroptical properties and redox activity.[1] The molecular engineering combining helicene chemistry with organometallic chemistry has recently been shown to give access to multi-functional chiral systems displaying strong optical activity associated with other functions provided by metal ions, for instance, redox activity and luminescence.[1,2] This new strategy has shown great potential for important optoelectronic applications such as chiral organic light-emitting diodes (OLEDs),[3a] transistors,[3b] chiral sensors,[3c]

chiroptical switches,[1k,2f-i,3c] motors,[3d,e] or non-linear optical (NLO) materials.[3f] Carbon-rich metal complexes such as metal-aryl-alkynyl complexes with d^6 metal centers (Ru(II), Fe(II)) display unique properties such as a facile electron transfer[4] which has enabled chemists to design new multi-functional molecular systems whose optical properties can be readily redox-triggered (NLO-activity,[4e,5a-e] luminescence,[5f-h] absorption and colour,[5i,j] circular dichroism[2f,h]). The aryl-alkynyl ligands are non-innocent.[4a,e,i] Accordingly, the electronic structure in the helical core of a π-conjugated helicene-alkynyl ligand is greatly modified by redox processes taking place at the metal, which can be readily observed by the accompanying changes in the electronic circular dichroism (ECD). There is now sizable literature on such ECD redox switching.[1k,2f,h,3c,6] However, an equivalent impact on the vibrational optical activity, namely vibrational circular dichroism (VCD)[7] and Raman optical activity (ROA),[8] has only recently been demonstrated. We recently reported the synthesis of new organometallic helicenes based on iron-alkynyl-carbo[6]helicenes that display unprecedented redox-triggered chiroptical switching activity (Scheme 1).[9] Upon oxidation, strong changes of vibrational modes, either local or extended coupled modes, were observed by VCD and ROA.
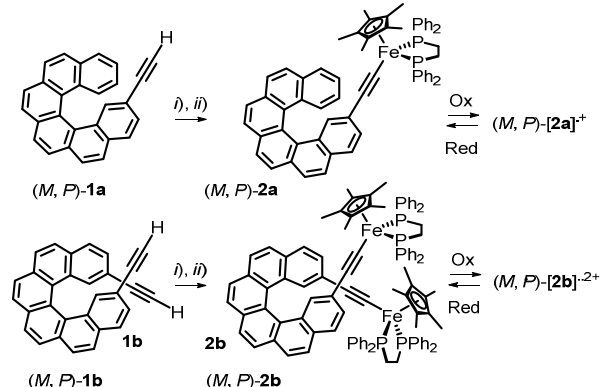
Scheme 1. Organometallic mono- and bis-iron-ethynyl-carbo[6]helicene derivatives **2a,b** obtained from mono- and bis-ethynyl-carbo[6]helicenes **1a,b**, and their redox-switching processes. *i*) Fe(κ^2-dppe)(η^5-C$_5$Me$_5$)Cl, MeOH, THF, NaPF$_6$; *ii*) THF, *t*BuOK.[9]

Herein, we present a complete account of our experimental and theoretical studies, including a detailed analysis of ECD and VCD spectra, with emphasis on the monometallic system **2a** because it was hardly discussed in our initial report.[9] Furthermore, for the first time, the ROA spectrum of an organometallic helicene species, *i.e.* **2a**, is calculated under resonance conditions, using a recently developed method,[10]

[a]   Dr. C. Shen, Dr. J. Crassous, Institut des Sciences Chimiques de Rennes UMR 6226, CNRS Université de Rennes 1, Campus de Beaulieu, 35042 Rennes Cedex (France).
        E-mail: jeanne.crassous@univ-rennes1.fr

[b]   Dr. M. Srebro-Hooper, Faculty of Chemistry, Jagiellonian University, Gronostajowa 2, 30-387 Krakow (Poland).

[c]   T. Weymuth, Dr. F. Krausbeck, Prof. M. Reiher, ETH Zürich, Laboratorium für Physikalische Chemie, Vladimir-Prelog-Weg 2, CH-8093 Zürich (Switzerland).

[d]   Dr. B. Nieto-Ortega, Prof. F. J. Ramírez, Prof. J. T. López Navarrete, Prof. J. Casado, Department of Physical Chemistry, University of Malaga, Campus de Teatinos s/n, Malaga 29071 (Spain).

[e]   Prof. J. Autschbach, Department of Chemistry, University at Buffalo, State University of New York, Buffalo, NY 14260 (USA). Email: jochena@buffalo.edu

        Supporting information for this article is given via a link at the end of the document.

and analysed with respect to the experiment. These resonance-ROA (RROA) calculations clearly indicate that a two-state model, which has in the past been successful to rationalize mono-signate RROA spectra, does not explain the intricate dependence of the RROA spectrum of **2a** as a function of the incident laser wavelength.

Results and Discussion

Helicene-ethynyl derivatives **2a** and **2b** grafted respectively with one or two electroactive [Fe(κ^2-dppe)(η^5-C$_5$Me$_5$)] fragments (dppe: 1,2-bis(diphenylphosphino)ethane, C$_5$Me$_5$: pentamethylcyclopentadienyl) were prepared from the organic precursors 2-ethynyl-carbo[6]helicene **1a** and 2,15-diethynyl-carbo[6]helicene **1b** by a recently described method (Scheme 1).[9,11] Introducing one or two electroactive "Fe(κ^2-dppe)(η^5-C$_5$Me$_5$)" units onto a helicene-alkynyl core significantly modifies its (chiro)optical and redox properties. The electronic π-interaction between iron and ethynyl-[6]helicene in **2a**,**b** was confirmed by UV-vis spectroscopy. The spectra display absorption bands between 300-330 nm that correspond mainly to ligand-centered π-π^* transitions that are similar to the ligands **1a**,**b** (ε ~ 20-30·10^3 M^{-1} cm^{-1}). However, there are two new broad low-energy bands at 390 and 480 nm with moderate magnitude that do not appear in the spectra of **1a**,**b** (ε ~ 7-16·10^3 M^{-1} cm^{-1}, see Figure S1 in the SI). In the following, changes of chiroptical properties of **2a**,**b** in the UV-visible (ECD and optical rotation (OR)) and infra-red (VCD) regions are presented in detail, where possible, relative to those of their helicenic organic precursors **1a**,**b**. A complete account of redox-triggered chiroptical tuning of **2a**,**b** observed via ECD, OR, VCD, and ROA is then provided.

ECD spectroscopy, OR, and electrochemical behaviour

The ECD spectra revealed a great impact of grafting an iron-ethynyl moiety onto the [6]-helicene core. As was previously shown,[2f,h] the 2-ethynyl-carbo[6]helicene ligand **1a** displays intense ECD in the UV-vis region (*P*-**1a**: 270 nm, $\Delta\varepsilon$ = -111 M^{-1} cm^{-1}; 332 nm, $\Delta\varepsilon$ = +188 M^{-1} cm^{-1} in CH$_2$Cl$_2$, Figure 1). In comparison, the ECD of *P*-**2a** shows (i) two strong negative ECD bands at 245 nm ($\Delta\varepsilon$ = -114 M^{-1} cm^{-1}) and 273 nm (-94 M^{-1} cm^{-1}), (ii) a set of three intense positive bands (probably corresponding to a vibronic progression) at 331 nm (+136 M^{-1} cm^{-1}), 350 nm (+92 M^{-1} cm^{-1}) and 385 nm (+34 M^{-1} cm^{-1}), and (iii) an additional very broad moderately intense positive band around 500 nm (+20 M^{-1} cm^{-1}). The spectra of bis-ethynyl-substituted enantiopure *M*- and *P*-**1b** undergo similarly strong modifications upon grafting two "Fe(κ^2-dppe)(η^5-C$_5$Me$_5$)" units, yielding ECD spectra for *M*- and *P*-**2b** that are similar to **2a** but with much stronger intensities for the new ECD-active bands around 400 and 500 nm (*P*-**2b**: $\Delta\varepsilon$ = +68 M^{-1} cm^{-1} at 506 nm, Figure 1).

Chiroptical properties of **2a**,**b** were calculated[12] with time-dependent density functional theory (TDDFT) following DFT geometry optimizations with BP/SV(P). For full computational details, including the number of calculated excitations per system and the line broadening, and for additional calculated data, see the SI (part 7: Computational Section). Two stable and energetically nearly degenerate conformers of **2a** (**2a-I** and **2a-II** in Figure 2) were obtained upon rotation of the helicene moiety around the alkynyl bond, with **2a-I** being similar to the solid-state structure[9] and slightly lower in energy. Only one stable

conformer was found for **2b**. The HOMOs of **2a**,**b** extend over the metal, the ethynyl moiety and the helicene cores, while the LUMOs are localized on the π-helical core (Figure 3 and SI). The calculated B3LYP/SV(P) ECD spectra of *P*-**2a**,**b** agree well with experiment (inset of Figure 1, Figure 4, and SI). For comparison, Figure S22 in the SI presents calculated ECD spectra of **2a**,**b** obtained with different DFT functionals.

An analysis of dominant excitations in the low- and medium-energy regions of the simulated spectra (see Figure 4b, Table 1, Figures S24-S26 and Tables S1-S2 in the SI) reveals that the strong positive ECD band around 350 nm of *P*-**2a** is caused by a number of excitations with high and moderate rotatory strengths. This band is assigned as predominantly due to a Fe-ethynyl-helicene→dppe charge transfer (CT) and intraligand (IL) π-π^* transition within the helicene fragment enhanced by metal-ethynyl orbital interactions. For instance, excitations #12 and #28 of *P*-**2a-I** afford the strongest positive rotatory strengths. They are calculated at 393 and 339 nm, respectively, with a dominant HOMO-to-LUMO+4 contribution (49%) for #12 where the LUMO+4 is centered on the dppe moiety (Table 1, Figures 3 and 4b, SI). For excitation #28, the dominant contributions are HOMO-4-to-LUMO (32%) and HOMO-3-to-LUMO+1 (29%) and involve helicene-centered MOs.

The broad ECD band around 500 nm is caused by excitations calculated between 480 and 550 nm that are mainly of Fe-ethynyl-helicene→helicene CT character (*P*-**2a-I**: #3, λ = 524 nm, HOMO-to-LUMO (96%); #4, λ = 488 nm, HOMO-to-LUMO+1 (72%)). The assignment of the ECD spectrum of the bis-iron complex *P*-**2b** (Figure S29, Table S5) is similar to that of the mono-iron system *P*-**2a**.[9] For *P*-**2b** the main positive ECD-active band is caused by excitations #29 and #32 calculated at 384 and 379 nm, respectively. The excitations are mainly assigned as Fe-ethynyl-(C$_5$Me$_5$)→helicene and Fe-ethynyl-helicene→helicene CT (HOMO-4-to-LUMO and HOMO-to-LUMO+12) with contributions from IL helicene π-π^* (#29, HOMO-6-to-LUMO+1) and Fe-ethynyl-helicene→dppe CT (#32, HOMO-to-LUMO+6). See Figure S30 in the SI for respective MOs of **2b**. The broad ECD band around 500 nm is caused by intense excitations #5 (λ = 496 nm) and #9 (462 nm) which are almost pure Fe-ethynyl-helicene→helicene CT (HOMO-1,HOMO-to-LUMO,LUMO+1).

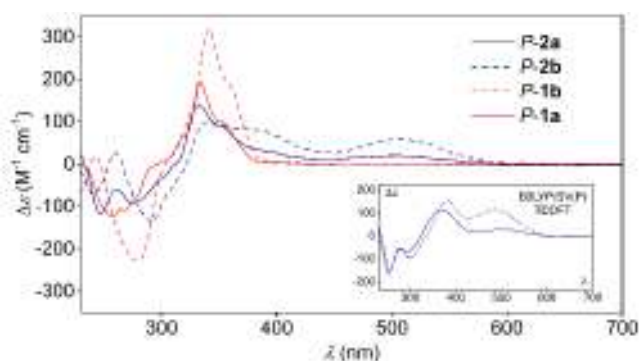**Figure 1.** ECD spectra of *P*-**1a** (plain red), *P*-**2a** (plain blue), *P*-**1b** (dashed red) and *P*-**2b** (dashed blue) in CH$_2$Cl$_2$ (*C* 1·10^{-5} M).[9] Inset: Simulated (B3LYP/SV(P)) spectra of *P*-**2a** and *P*-**2b** (see also SI).
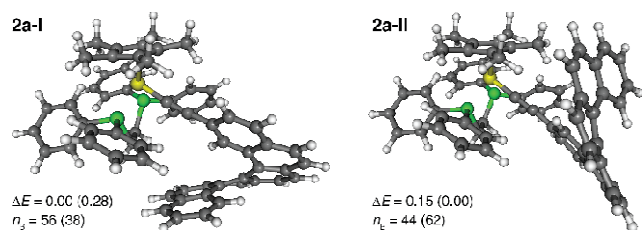
Figure 2. Two optimized (BP/SV(P)) structures of **2a** along with their relative energy values (ΔE, in kcal/mol) with respect to the lowest-energy conformer and the corresponding Boltzmann populations (n_B, in %). In parentheses, BP/SV(P) ΔE and n_B for the corresponding oxidized species [**2a**]$^{\bullet+}$ are given.
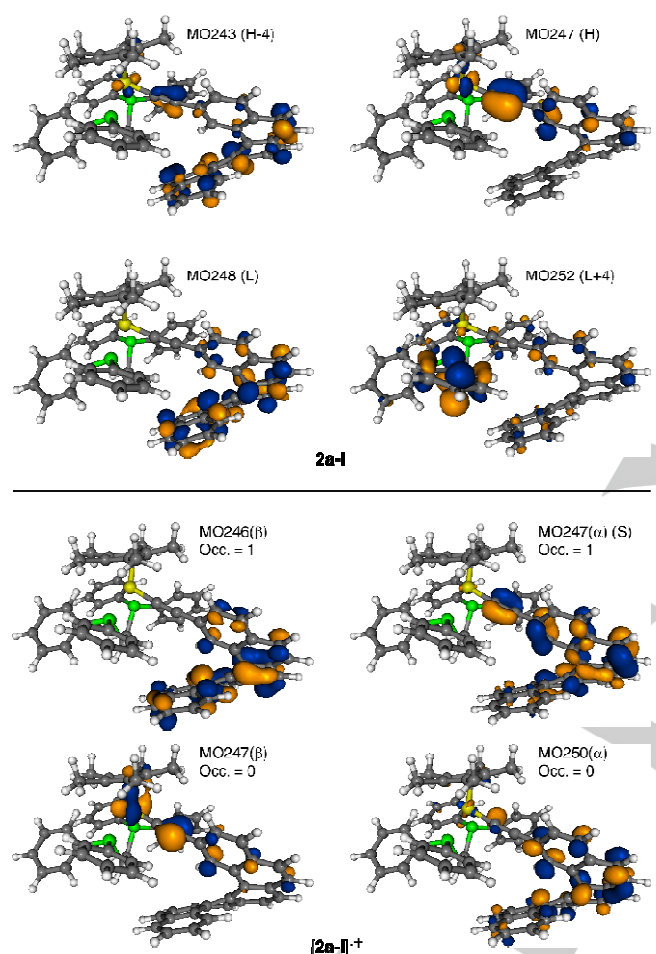

Figure 3. Isosurfaces (±0.04 au) of MOs involved in selected electronic excitations of **2a**/[**2a**]$^{\bullet+}$ (conformer I). 'H' = HOMO, 'L' = LUMO, 'S' = SOMO. The corresponding MOs for **2b**/[**2b**]$^{\bullet\bullet2+}$ can be found in Ref. [9]. See also SI for a full set of MOs for both systems.

Overall, the analysis shows that the participation of orbitals from iron itself, or from its ancillary ligands (dppe, C$_5$Me$_5$), has a strong impact on the ECD spectra of *P*-**2a**,**b**. In particular, the additional ECD bands at long wavelengths have large contributions from the metal center and are responsible for a three-fold increase of the molar rotation (MR) of **2a** relative to the organic precursor **1a** (*P*-**1a**: $[\Phi]_D^{23}$ = +11030° cm^2/dmol (calc.[2f,h] BHLYP/SV(P) +17002), *P*-**2a**: $[\Phi]_D^{23}$ = +35800° cm^2/dmol (calc. +43073)). **2b** has an even larger molar rotation (*P*-**2b**: $[\Phi]_D^{23}$ = +79700° cm^2/dmol (calc. +83844)), four times that

of **1b** (*P*-**1b**: $[\Phi]_D^{23}$ = +20000° cm^2/dmol (calc.[2f,h] +22230). In both cases, the number of helicene cores is the same in the product and the precursor. Evidently, grafting Fe^{II}-fragment(s) in conjugated position onto a [6]helicene platform substantially increases its optical activity. The effect is considerably stronger than previously reported for Ru^{II}-vinyl-[6]helicene complexes.[2f,h] The stronger effect for **2a**,**b** is obtained because the sodium-D wavelength (589 nm) is in the tail of an ECD band and therefore the MR is enhanced by the proximity to an electronic resonance (Figure 1, inset, SI). A similar situation is found for the Raman optical activity spectra which are particularly intense given the resonant enhancement by exciting with a 532 nm Raman laser (*vide infra*).

The electroactive properties of organometallic helicenes **2a**,**b** were also examined. Cyclic voltammetry (CV) studies of complex **2a** (CH$_2$Cl$_2$/NBu$_4$PF$_6$, 0.2 M) revealed the presence of one chemically and electrochemically reversible oxidation at E$_1$° = -0.604 V (100 mV·s^{-1}) *vs.* the ferrocene/ferrocenium (Fc/Fc$^+$, see Figure S3) internal reference (E$_1$° = -0.144 V *vs.* SCE), which corresponds to one-electron oxidation affording [**2a**]$^{\bullet+}$.[4,9] Since **2b** bears two redox active moieties, the bis(Fe^{II}-ethynyl)-[6]helicene is therefore a good system to investigate the impact of multi-oxidation processes on the prototype [6]helicene fragment. Two consecutive reversible one-electron oxidation waves were observed in CH$_2$Cl$_2$ at E$_1$° = -0.640 V and E$_2$° = -0.549 V *vs.* the Fc/Fc$^+$ (see Figure S4, E$_1$° = -0.180 V and E$_2$° = -0.089V *vs.* SCE). The appearance of the two waves, instead of one, but separated by ~ 91 mV suggests that the two iron centers interact, most likely due to electrostatic repulsion between charges of the same sign and – potentially – via conjugation through the helicene. Solvation energy changes or ion pairing may also account for the presence of the two oxidation waves in **2b**.[4] Note that the two oxidation potentials are too close to obtain the mono-radical cation [**2b**]$^{\bullet+}$ in a pure form due to substantial comproportionation. Indeed, a comproportionation constant K$_c$ = 35 is estimated and corresponds to the presence of a maximum of *ca.* 75% of the total amount of the species in equilibrium coming from [**2b**]$^{\bullet+}$.[4a,g,9]
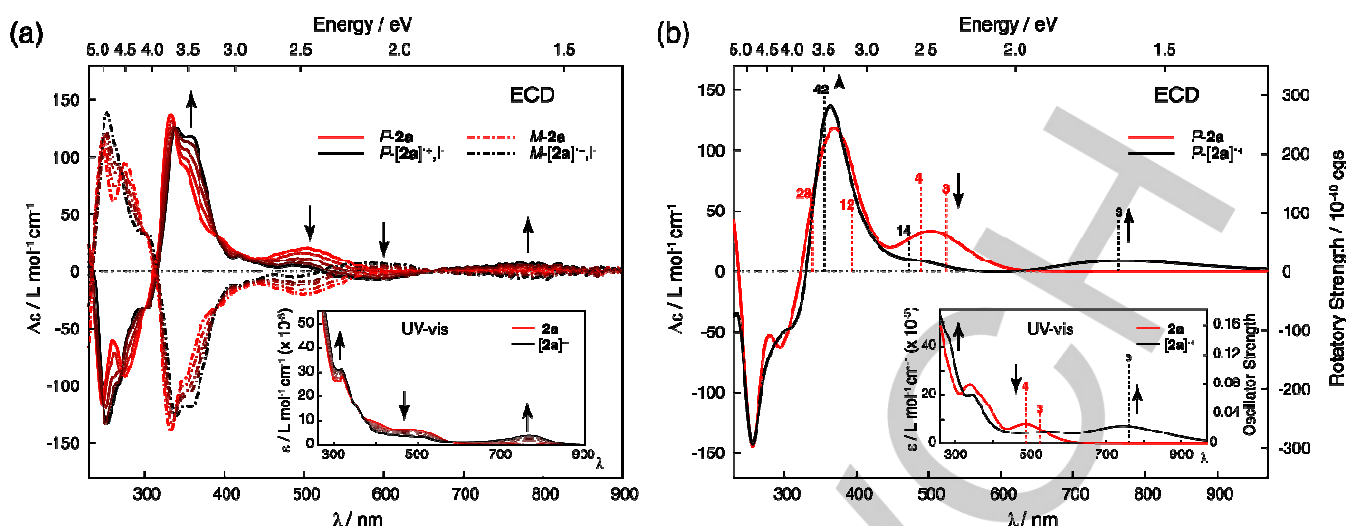
3

Figure 4. (a) Evolution of the ECD spectrum of **2a** upon its oxidation with iodine. ECD spectra of *P*-**2a** (plain red), oxidized species *P*-[**2a**]•+,I⁻ (plain black) and their corresponding enantiomers *M*-**2a** and *M*-[**2a**]•+,I⁻ (dotted lines) in CH₂Cl₂ (*C* 10⁻⁵ M). Inset: Spectroelectrochemical oxidation studies of **2a** with potentials from -0.2 to +0.4 V (*vs*. Ag pseudo-electrode) in C₂H₄Cl₂, NBu₄PF₆ (0.2 M).[9] (b) Simulated (B3LYP/SV(P), Boltzmann-averaged for two conformers) ECD spectra of *P*-**2a** (red line) and *P*-[**2a**]•+ (black line). Inset: The corresponding UV-vis spectra. No spectral shift was applied. Calculated excitation energies and rotatory / oscillator strengths indicated as 'stick' spectra. Numbered excitations for the lowest-energy conformers for each species (respectively, **2a-I** and [**2a-II**]•+) were analyzed in detail (see Table 1 and SI).

Table 1. Selected dominant excitations and occupied (occ) – unoccupied (unocc) MO pair contributions (greater than 10%) of *P*-**2a** and *P*-[**2a**]•+ in their energetically preferred conformations. See also Tables S2 and S3 in the SI.

Excitation	E [eV]	λ [nm]	f	R [10⁻⁴⁰ cgs]	occ no.	unocc no.	[%]
P-**2a-I**							
#3	2.37	524	0.0416	131.02	247	248	96.0
#4	2.54	488	0.0707	148.10	247	249	72.0
#12	3.15	393	0.1100	105.38	247	252	49.1
					247	255	10.9
#28	3.66	339	0.1759	121.93	243	248	32.1
					244	249	29.1
P-[**2a-II**]•+							
#1	0.56	2201	0.0014	31.39	242(β)	247(β)	45.9
					241(β)	247(β)	18.3
					244(β)	247(β)	13.5
#2	0.92	1344	0.0006	13.82	241(β)	247(β)	32.1
					242(β)	247(β)	15.4
					236(β)	247(β)	11.6
					237(β)	247(β)	10.1
#3	1.62	763	0.1060	88.90	245(β)	247(β)	58.8
					246(β)	247(β)	23.6
#14	2.62	473	0.0131	50.13	234(β)	247(β)	12.0
					232(β)	247(β)	10.6
#42	3.49	355	0.0844	298.55	246(α)	251(α)	15.6
					246(β)	251(β)	12.5

Electron Paramagnetic Resonance (EPR) experiments and magnetic susceptibility measurements of the mono- and di-radical cations [**2a**]•+ and [**2b**]••2+ (generated from **2a** and **2b** by using, respectively, 0.5 and 1 equiv. of iodine as a chemical oxidant) had recently shown that the charge was mainly localized on the iron center(s).[9,11] Further analyses of the electronic structure of the mono-oxidized species [**2a**]•+ (spin doublet) and the bis-oxidized species [**2b**]••2+ were performed (B3LYP/SV(P)//BP/SV(P)). We modelled [**2b**]••2+ in a spin triplet configuration as well as in an open-shell singlet; the latter corresponds in the DFT calculation to a broken-symmetry solution (due to the use of a single reference in Kohn-Sham DFT). As seen in Figures 5 and S32, the unpaired electron density is spread out over the metal centers and on the helicene π-system via the ethynyl bridges with alternating positive / negative spin density at the carbon atoms of the conjugated system *i.e.* alternating localization of excess α-spin / β-spin density, which is not unexpected.[11c,d] The densities of the singly occupied molecular orbitals (SOMOs) of [**2a**]•+, MO247(α), and [**2b**]••2+, MO407(α) and MO408(α) of the triplet, (Figure 3 and Figures S28 and S31 in the SI) do not correspond to the total electron spin density as, due to relaxation and spin polarization relative to the neutral systems, they are centered on helicene-alkynyl moiety with negligible metal orbital contribution. However, the unoccupied counterparts, MO247(β), and MO407(β)-MO408(β), respectively, demonstrate essentially the same characteristics as the HOMO of the neutral **2a**,**b** systems,[11c] as well as the calculated spin density distribution and therefore these orbitals represent the "electron holes" in the β-spin density.

From the experimental and theoretical data for the radical species [**2a**]•+ and [**2b**]••2+, one can conclude that each iron center is efficiently interacting with the helicene ligands through each ethynyl bridge. However the two iron centers do not electronically interact with each other to a significant degree in [**2b**]••2+ and therefore the di-radical most likely exists in a mixture of spin singlet and triplet states. This conclusion is supported by the energetic degeneracy of open-shell singlet and triplet states of the doubly oxidized species of **2b** from DFT calculations, and by the experimental magnetic data discussed elsewhere.[9] Therefore the electrochemical separation of 91 mV between the two oxidation waves in [**2b**]••2+ can be attributed to electrostatic repulsion more than to a long-range through-bond interaction which would magnetically couple the two spins and create an

energy gap between the relevant singlet and triplet states. Unlike the former ruthenium-vinyl-carbo[6]helicene derivatives,[2f,h] the iron-ethynyl-carbo[6]helicene organometallic complexes appear stable enough, even in the oxidized states, to be studied by a great variety of optical and chiroptical spectroscopies.

The one- or two-electron oxidation processes of **2a**→[**2a**]•+ and **2b** →[**2b**]••2+, respectively, were monitored by UV/vis/NIR and ECD spectroscopy either in an optically transparent thin-layer electrochemical (OTTLE) cell ($C_2H_4Cl_2$/NBu_4PF_6, 0.2 M) upon oxidation at +0.4 V *vs.* a Ag pseudo-potential electrode or by using iodine as chemical oxidant in CH_2Cl_2. The UV/vis/NIR spectroelectrochemical studies of **2a** revealed an increase of the high energy bands (< 380 nm), a slight decrease of the bands between 380-580 nm, the appearance of a lower-energy broad absorption band at ~780 nm of moderate intensity (ε ~ 4·10^3 M^{-1} cm^{-1}), see Figure 4a, inset, and an NIR band between 1300-2100 nm of very low intensity (ε ~ 170 M^{-1} cm^{-1}), compare with Figure S6. Full reversibility was observed upon several oxidation / reduction cycles (see Figure S17 in the SI). The chemical oxidation of **2a** was also performed using iodine and demonstrated the same UV/vis/NIR spectroscopic characteristics (Figures S5 and S6 in the SI), confirming a clean chemical oxidation of **2a** into [**2a**]•+.

For complex **2b**, the UV/vis/NIR spectroelectrochemistry or chemical iodine oxidation showed that several bands undergo changes during the first oxidation stage at +0.2 V (*vs.* Pt electrode), with an increase of the band between 230-350 nm, a decrease of the bands between 350-550 nm, and the appearance of a broad band around 650-850 nm. Upon further oxidation (potential increased from +0.2 to +0.4 V), all these bands (450-600 nm and 850 nm) disappeared and a new band grew at 750 nm (see Figure S7 in the SI). Finally, a NIR absorption band of very low intensity (ε ~ 255 M^{-1} cm^{-1}) was found between 1300-2100 nm (see Figure S8).
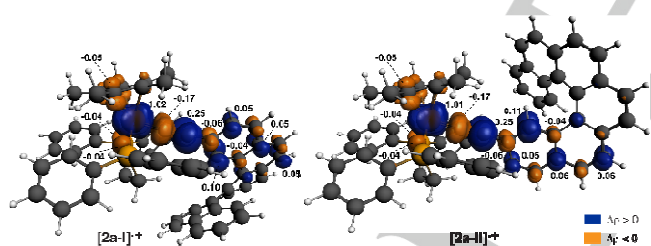

Figure 5. B3LYP/SV(P) electron spin density, $\Delta\rho = \rho^\alpha - \rho^\beta$ (±0.0015 au isosurfaces), of [**2a**]•+ (spin-doublet, two conformers). Numbers listed are Mulliken spin populations. The corresponding spin density for [**2b**]••2+ can be found in Ref. [9] and in Figure S32 in the SI.

Having established that **2a,b** undergo reversible oxidation processes, the next step towards electrochemical chiroptical switches was to investigate whether these redox processes affect their chiroptical behavior. The ECD spectra of *P*-**2a** and *P*-[**2a**]•+,I$^-$ in CH_2Cl_2, displayed in Figures 4a, show that the bands are strongly modified. For example, upon oxidation of *P*-**2a**, *i*) the intense positive band around 360 nm significantly increases from $\Delta\varepsilon$ = +70 to +118 M^{-1} cm^{-1}, *ii*) the positive band between 450-600 nm decreases and gains a positive-negative feature at 490 and 585 nm of low intensity ($\Delta\varepsilon$ ~ +7 and -5 M^{-1} cm^{-1}, respectively), and *iii*) a new positive band of low intensity appears in the NIR region (between 680-880 nm, $\Delta\varepsilon$ ~ +5 M^{-1} cm^{-1}). Along with the changes in the ECD spectra, the molar

rotation undergoes a strong decrease upon oxidation of **2a** (*P*-**2a**: $[\Phi]_D^{23}$ = 35800° cm^2/dmol → *P*-[**2a**]•+,I$^-$: $[\Phi]_D^{23}$ = +9860° cm^2/dmol in CH_2Cl_2, see Table S7 in the SI for calculated data). This may be explained partially by the appearance of the negative ECD band in the 500-600 nm region which has a compensating effect on the optical rotation. Exploiting these modifications, along with the reversibility of the oxidation process, allows for obtaining an electrochemical chiroptical switch.[2f,h,3c,6] Indeed, by stepping oxidation and reduction potentials around +0.4 V and -0.4 of a dichloromethane solution of **2a** (0.2 M, NBu_4PF_6) in an OTTLE cell leads to a reversible modulation of the ECD signals as illustrated at 589 nm where the $\Delta\varepsilon$ changes sign from +2 to -5 M^{-1} cm^{-1} (see Figure S19 in the SI). As for mono-Fe complex **2a**, the formation of *P*-[**2b**]•+ and *P*-[**2b**]••2+ was also monitored by ECD spectroscopy either in an OTTLE cell or by chemical oxidation with iodine. Again, net differences between ECD spectra of oxidized species and the neutral system, very similar to those described for **2a**/[**2a**]•+,I$^-$, although visibly enhanced due to a presence of two metal centers, were observed (see Figures S13-S16 in the SI). In particular, there is a strong increase of the positive ECD band around 350 nm (($\Delta(\Delta\varepsilon)$ > +100 M^{-1} cm^{-1} at 372 nm) and a strong decrease of the positive band between 530-650 nm with the appearance of a clear negative band for *P*-[**2b**]••2+ (note that for mono-oxidized species *P*-[**2b**]•+ the intensity of the band only undergoes a decrease.) In addition, a clear broad band appears in the vis/NIR (670-900 nm) on *P*-**2b**→*P*-[**2b**]••2+ ($\Delta(\Delta\varepsilon)$ ~ +20 M^{-1} cm^{-1} at 767 nm). Such as for **2a**, the *D*-line molar rotation of **2b** decreases strongly upon oxidation reflecting the significant changes in the ECD spectrum at this energy region when going from **2b** to [**2b**]••2+ (*P*-**2b**: $[\Phi]_D^{23}$ = +79700 °cm^2/dmol → *P*-[**2b**]••2+,2I$^-$: $[\Phi]_D^{23}$ = +8990 °cm^2/dmol in CH_2Cl_2, see Table S7 in the SI for calculated data).

It is important to note that the system can be used as redox chiroptical switch either at short wavelengths / high energies, which belongs to the classic CD-active fingerprint of helicene derivatives ($\Delta(\Delta\varepsilon)$ > +100 M^{-1} cm^{-1} at 372 nm for *P*-**2b**), or at a long wavelength / small energies, which is due to the presence of the Fe-center (*vide infra*) (($\Delta(\Delta\varepsilon)$ ~ +20 M^{-1} cm^{-1} at 767 nm) upon stepping potentials between -0.4 and +0.4 V by reversibly interconverting *P*-**2b** and *P*-[**2b**]••2+ (see Figure S15). Furthermore, note that we have previously observed strong modifications and inversion of the signs of the molar rotation values at 1.54 µm upon oxidation of *M*-**2a**→*M*-[**2a**]•+ and *M*-**2b**→*M*-[**2b**]••2+. Consequently, the systems constitute a new type of redox-triggered chiroptical switch using an additional output read-out at 1.54 microns *i.e.* outside the more common wavelength regions explored in laboratory settings, but instead at wavelengths that are commonly used for fiber-optics telecommunication.[9]

The modifications of ECD spectra for both *P*-**2a**/*P*-[**2a**]•+ and *P*-**2b**/*P*-[**2b**]••2+ that appear in the UV/vis/NIR regions are very well reproduced by TDDFT B3LYP calculations, as illustrated in Figure 4b and in Figure S29, respectively. Based on the detailed analysis of selected dominant excitations of [**2a**]•+ and [**2b**]••2+ (triplet) the changes in ECD bands of the neutral complexes **2a** and **2b** observed upon metal oxidation are mostly due to the presence of contributions involving the orbitals representing the electron holes in the β-spin density as well as a change in the character of the SOMO(α) compared with their doubly occupied counterparts of the neutral species (Figures 3 and 4b, Table 1, and SI).[2h] For example, the positive NIR ECD intensity observed around 700 nm in the oxidized species originates from

excitations assigned as helicene→Fe-ethynyl-helicene intraligand/ligand-to-metal (IL/LM) CT transitions involving the electron hole orbital(s); see excitation #3 in the case of [**2a**-II]^{•+} (763 nm, MO245(β),MO246(β)-to-MO247(β)) and excitations #5 and #6 for [**2b**]^{••2+} (~668 nm, MO405(β),MO406(β)-to-MO407(β),MO408(β)). The main positive band around 350 nm is caused by a number of excitations assigned predominantly as IL π-π* transitions within (ethynyl-)helicene fragment mixed with Fe-dppe-(C₅Me₅)→Fe-ethynyl-helicene CT of LM character and / or ethynyl-helicene→Fe-dppe-(C₅Me₅) LM CT. For instance, excitation #42 of *P*-[**2a**-II]^{•+} with the strongest positive rotatory strength calculated at 355 nm has the largest contributions from helicene-centered MO246(α)-to-MO251(α) and MO246(β)-to-MO251(β) transitions. In the case of *P*-[**2b**]^{••2+} the band is mainly caused by excitations #59 (382 nm) and #67 (367 nm), involving MOs localized in (ethynyl-)helicene moiety (for example MO405(β)-MO410(β) and MO407(α)-MO412(α) pairs) and excitation #62 (369 nm) which corresponds to dppe→Fe-ethynyl-helicene (MO392(β)-to-MO407(β)) CT (see Tables 1 and S6 for details).

Our explanation is that due to the oxidation, there is a lesser involvement, on average, of metal orbitals in these excitations, but increased involvement of 'helical' helicene π-orbitals that supports large rotatory strengths, thus rationalizing the increase of ECD intensity at these wavelengths. Visual inspection of the molecular orbitals involved in the relevant transitions of the oxidized systems [**2a**]^{•+} and [**2b**]^{••2+} indeed shows that overall contributions of Fe orbitals are decreased as compared to neutral species, especially in the case of ethynyl-helicene-type MOs. Similarly, a decrease in the intensity of the ECD band around 500 nm upon oxidation of both **2a** and **2b** can be accounted for the changes in the character of the underlying dominant excitations. In the case of the neutral systems, the band originates from Fe-ethynyl-helicene→helicene CT. Upon oxidation, the excitations become mostly helicene-centered and mixed with dppe,(C₅Me₅)→Fe-ethynyl-helicene and helicene→Fe-ethynyl-helicene LM/LL CT. The increased involvement of helicene orbitals is counter-balanced here by a loss in CT character affecting the electric transition dipole. Finally, the ECD intensity observed in the telecommunication domain (calculated between 1300-2500 nm, see for example excitations #1 and #2 in Table 1 for *P*-[**2a**]^{•+}, and the SI for *P*-[**2b**]^{••2+}) corresponds to Fe-ethynyl-centered transitions (with some helicene→Fe-ethynyl LM CT character) mixed with Fe-(C₅Me₅)→Fe-ethynyl MM/LM CT which again involve the electron hole orbitals of the oxidized species.

VCD spectroscopy

Apart from electronic CD and optical rotation, vibrational optical activity, *i.e*. VCD and ROA, may provide additional information related to the chirality and the redox switching, such as how the molecular vibrational modes are modified upon oxidation of the organometallic helicenes.[7,8] These vibrational optical activity techniques give unique insights into structure-spectroscopic relationships. Whereas quantum modelling of the ECD excitations of chiral organometallic systems is nowadays well known, quantum-chemical calculations of the VCD and in particular ROA and resonant ROA are much more challenging targets, by which their implementation in this paper represents a significant novelty in the field. Figure 6 shows how the IR and VCD spectra are modified upon oxidation of enantiopure

complexes *M*-/*P*-**2a** to *M*-/*P*-[**2a**]^{•+}. For instance, iron-ethynyl-complexes *M*-/*P*-**2a** show several interesting spectroscopic features: *i*) a strong IR and VCD-active band at 2048 cm⁻¹ corresponding to the C≡C stretch, with positive VCD sign for the *P* enantiomer (respectively negative for the *M*), *ii*) a sequence of positive-negative-positive signatures at respectively 1612-1595-1574 cm⁻¹ for the *P* enantiomer (of opposite signs for the *M*). These latter VCD patterns are typical of C=C stretching modes coupled with CCH bending vibrations and are similar to previously reported VCD spectra of ruthenium-vinyl-[6]helicene derivatives.[2h] For comparison, similar VCD-active bands are observed in organic helicenes, such as for example in 2-bromo-hexahelicene, where the breathing/CC stretching type modes appear as signals of alternated signs above 1550 cm⁻¹.[7b] Upon chemical oxidation with iodine, the C≡C stretching band moves to lower wavenumbers and splits (2035 and 1991 cm⁻¹), possibly due to Fermi coupling,[11b] with respectively a negative-positive VCD signature for the *P* enantiomer. Such wavenumber decrease is likely the result of the delocalization of the positive charge from the iron center into the acetylene bridge which thus acquires some cumulenic C=C=Fe character. Further, an 85-fold increase of the dissymmetry factor is observed upon oxidation (*g* = Δ𝜀/𝜀 from 7·10⁻⁵ to 6·10⁻³). Note that organic helicenes typically show dissymmetry factors of 10⁻⁴. This enhancement emphasizes the placement of the unpaired electron density within the C≡C moiety which gives rise to much stronger magnetic transition dipole moments for the vibrational transitions.[14] Important modifications, although of smaller impact on the intensities, are also observed in the 1600-1400 cm⁻¹ region which is dominated by C=C stretching modes coupled with CCH bending modes. These modifications are tentatively assigned to mechanical coupling of these skeletal vibrations with that of the cumulene-like fragment. Note that similar results are obtained for the bismetallic complex.[9]

The experimentally observed IR/VCD features of neutral species are qualitatively reproduced by the calculations (Figure 7, Figures S33 and S36 in the SI). In particular, a strong IR and VCD-active band corresponding to the C≡C stretching mode is computed at higher wavenumbers close to experimental values. Furthermore, the quantum-chemical vibrational analysis supports 'helicene' assignments of IR/VCD signals between 1600 and 1400 cm⁻¹. For oxidized species the agreement between calculated and experimental IR and VCD spectra is less satisfactory, especially for VCD (Figures S33 and S36 in the SI). However, an energetic shift and increase in intensity of the IR C≡C stretching band upon oxidation (along with its splitting for the mono-iron complex) seems to be correctly reproduced via theory.

While the application of VCD spectroscopy has become quite common in helicene chemistry for the determination of absolute configurations, or in conjunction with computational models, it has never been used for studying the effect of changing the electronic structure of a helicenic structure.[9] This has been possible here thanks to the high stability of iron-alkynyl complexes and their ability to be oxidized by a chemical reagent such as iodine.
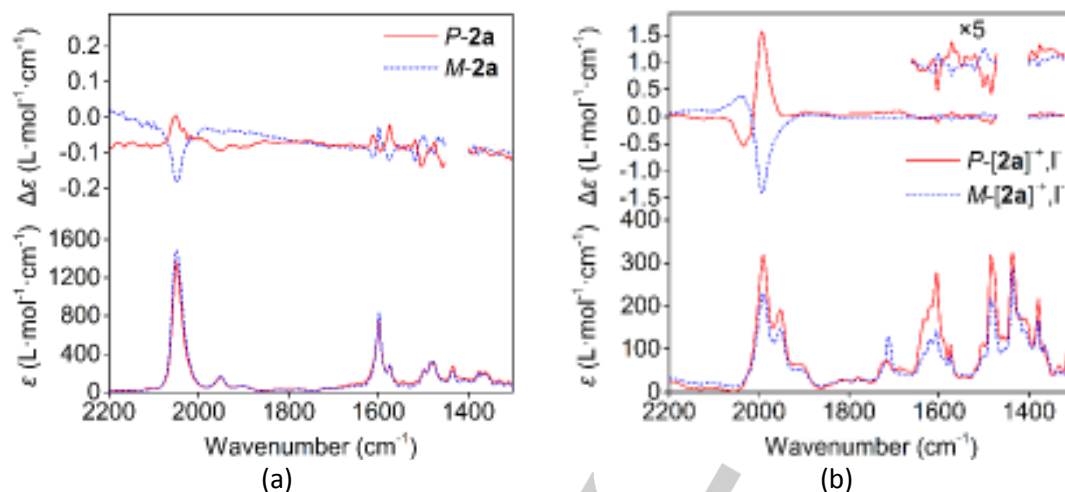
Figure 6. (a) VCD spectra (up) and IR spectra (down) for *P*-**2a** (red solid) and *M*-**2a** (blue dashed). (b) VCD spectra (up) and IR spectra (down) of *P*-[**2a**]$^{•+}$,I$^-$ (red solid) and *M*-[**2a**]$^{•+}$,I$^-$ (blue dashed). Noticeable different intensities in the IR spectra in *P*- and *M*-[**2a**]$^{•+}$,I$^-$ may be due to concentration errors and uncomplete oxidation upon I$_2$ addition. See Ref. [9] for the corresponding data for **2b**/[**2b**]$^{••2+}$.
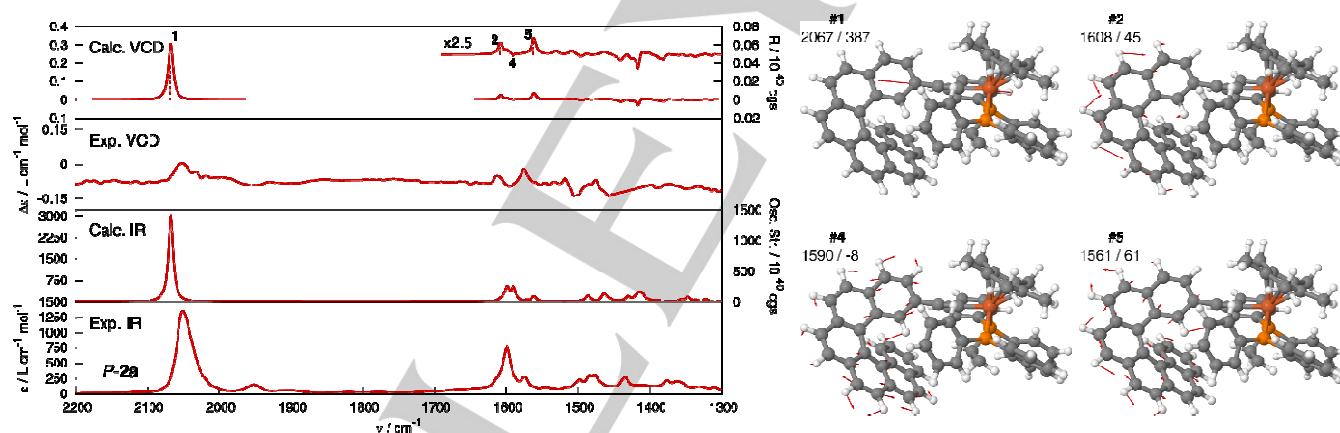

Figure 7. Left: Comparison of experimental and calculated (B3LYP/SV(P) gas-phase, frequencies scaled by 0.96, Boltzmann-averaged for two conformers) IR (down) and VCD (up) spectra of **2a**. Numbered VCD vibrations correspond to those analyzed in detail for **2a-I**. Right: Atomic displacement for the numbered normal modes in **2a-I**. Numbers listed are the corresponding vibrational frequency (in cm^{-1}, scaled) / rotatory strength (10^{-44} cgs) values. See also SI.

ROA spectroscopy

Raman optical activity measures the difference of the Raman scattered intensity between right and left circularly polarized light and has become one of the prime technique for determining absolute configurations of molecules[17-20] and conformers of biomolecules[21,22] in addition to ECD, VCD, and OR.[23,12] quantum-mechanical calculations have shown to be highly important for the assignment of ROA spectra, for instance to assign the absolute configuration of chirally deuterated neopentane[24] and methyloxirane in gas and liquid phases,[25,26] or the asymmetric carbon in CHFClBr.[27] Due to the weakness of the ROA signal under off-resonance conditions, there is an increasing interest in resonance ROA (RROA) within the

experimental and theoretical community.[10,28] According to a two-state approximation and TDDFT calculations for a small molecule under full resonance,[16] the RROA intensities are mono-signate, with the opposite sign of the ECD signal at the incident wavelength. Under near-resonance conditions, or when multiple electronic excitations influence the RROA intensity, or when vibronic effects are large,[16,28] the spectral pattern can become more intricate and remain weakly bi-signate.

To date, (resonance) Raman and ROA spectroscopy,[13] which are complementary techniques to IR and VCD, are far less utilized in helicene chemistry.[8] Herein it is described only the second example of ROA measurements on a helicene

7

system, besides the Johannessen et al. study of enantiopure *M*- and *P*-2-bromohelicene,[8a] which displays mirror-image ROA spectra with a strong signature corresponding to a D-mode that is reminiscent of coronene or graphene modes.[15] In our case (see Figure 8), three modes are strongly Raman active, *i.e.* for example for **2a**, we observe a G-mode (graphene-like CC stretching mode) at 1575 cm^{-1} and a D-mode (diamond-like CC breathing mode) at 1355 cm^{-1}, along with the C≡C stretching

mode at 2048 cm^{-1}. Several features are worth to note. As shown in Figure 8, all ROA bands display the same sign (that *i.e.* all negative for the *P* enantiomers and all positive for the *M* ones).[16] The experimental wavelength (532 nm) used for the measurements coincides with an electronic absorption band of the spectra for both **2a** and **2b**, which implies that what we observe is predominantly RROA. However, as shown below the situation is more intricate.
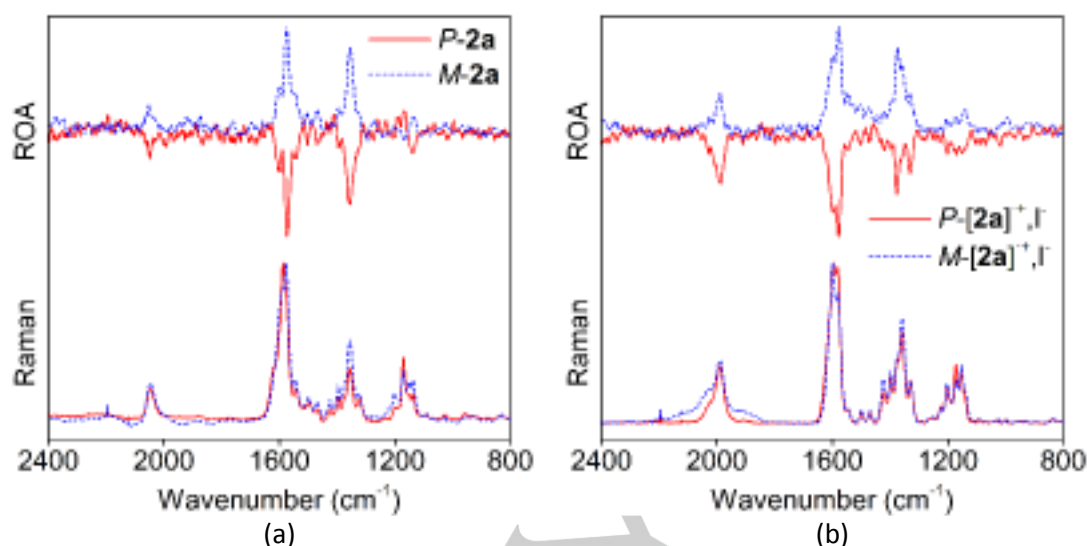

Figure 8. (a) ROA spectra (top) and Raman spectra (bottom) for *P*-**2a** (red solid) and *M*-**2a** (blue dashed). (b) ROA spectra (top) and Raman spectra (bottom) for *P*-[**2a**]$^{•+}$,I$^-$ (red solid) and *M*-[**2a**]$^{•+}$,I$^-$ (blue dashed). See Ref. [9] for the corresponding data for **2b**/[**2b**]$^{••2+}$.

Again, chemical oxidation reveals significant modifications of the Raman and ROA spectra, and shows that not only the C≡C stretching mode is affected upon oxidation (changing from 2048 to 1988 cm^{-1}) but also the G- and D-modes (see Figure 8) confirming to some extend the alternation of the π−conjugated paths. This finding is readily explained by the fact that the oxidation generates significant variations of the electronic structure also within the helicene core.

A new implementation for TDDFT RROA calculations developed recently[10] enabled us to compute for the first time the ROA spectrum of an organometallic helicene species, *i.e.* **2a**, and to study how it is affected by the resonance effects. The two conformers of **2a** are isoenergetic, and the RROA spectra are not expected to be affected much by the rotation of the helicene moiety about the Fe–C bond. Due to the high demand on computational resources, calculations were therefore performed for one of the conformers (II), which was chosen arbitrarily.

Since the calculated vs. experimental absorption wavelength relative to the experimental laser wavelength (532 nm) are likely to differ somewhat, a scan of the appearance of the calculated ROA spectrum of **2a** as a function of the laser wavelength used in the linear response calculations was performed, using wavelengths between 490 and 580 nm. All calculated ROA spectra are provided in the SI along with the corresponding Raman spectra (Figures S39-S50 and Figures S54-S65 in the SI). The calculation with λ = 540 nm overall agrees best with the experiment. The laser wavelength difference between this calculation and the experiment is very small. The calculated and experimental RROA are compared in Figure 9 for *M*-**2a** which

features predominantly positive ROA across the spectral range. We first observe that the calculated RROA spectrum for an incident wavelength of λ = 540 nm is nearly completely mono-signate. *I.e.*, according to the two-state model prediction of positive ROA for resonance with the negative long-wavelength ECD band of *M*-**2a** the spectrum appears to be under full or very close to resonance. Chiroptical intensities are generally not easy to reproduce by calculations, and therefore the agreement of the calculations and the experiment is quite satisfactory. In terms of the relative intensity of the G- vs. D-mode bands, the calculations predict the former to be weaker than the latter, which is similar to the experimental ROA of bromohelicene, whereas experimentally for the D-modes are less intense than the G-modes. The discrepancy may in part be due to the neglect of medium effects in the calculations.

Four distinct RROA features can be identified, labelled as 1 to 4 in Figure 9. Peak 4 corresponds to the alkynyl stretching mode. This mode, in particular, appears to be sensitive to the incident wavelength and changes its sign around λ = 530 nm (see Figures S44-S46 in the SI). For λ = 580 to 560 nm, the alkynyl peak is positive and very intense. It becomes weakly negative at 532 nm and increases in negative intensity toward shorter wavelengths. Peaks 3 and 1 correspond to graphene-like G- and D-modes, respectively. These bands are prominent in the ROA spectrum across the scanned laser frequency range. The modes underlying the weaker band 2 are characterized by CH bending vibrations across the whole molecule and CH bending vibrations solely in the helicene substructure.

While there are individual vibrational transitions in *M*-**2a** with negative ROA intensity they do not influence the overall positive sign of the broadened spectrum in the peak 1 to 3 frequency range. At laser wavelengths above 530 nm, the ROA for these modes is not strongly enhanced, but the relative peak intensities and the overall intensity increase significantly as the laser wavelength becomes near-resonant (but not fully resonant) with ECD bands that are dominated by helicene-centered transitions with strong rotatory strengths. However, it is important to note that the strong G- and D-mode bands are essentially mono-signate even for off-resonance wavelengths. This finding is in agreement with the study of 2-bromo-[6]helicene by Johannessen et al.[8a] The calculations further predict a bi-signate ROA spectrum for incident laser wavelengths below 530 nm, with the alkynyl peak becoming negative while the other peaks remain positive. In the calculated Raman Spectra (Figures S54-S65), the alkynyl stretch is the most intense transition at long wavelengths and only gradually decreases in intensity as the incident laser wavelength decreases. The different appearance of the ROA and Raman spectra in the resonant regimes is an indication that multiple excited states influence the ROA spectrum.

We attribute the curious sign and intensity changes of the alkynyl stretch ROA signal as a function of the incident wavelength to resonance / near-resonance influences from a pair of very weak and weak electronic transitions (#1, λ = 564 nm, R = -2.2·10^{-40} cgs, and #2, λ = 549 nm, R = +11.8·10^{-40} cgs, for the chosen *M*-**2a** conformer) that are localized at the metal, ligands other than the helicene, and the alkynyl group, which are competing with much more intense helicene- and alkynyl-helicene-centered electronic transitions with mostly negative signs of the rotatory strength at shorter wavelengths, starting with #3, λ = 505 nm, R = -142.8·10^{-40} cgs (see Figure S53). An analysis of the RROA intensity of the alkynyl stretching mode in terms of atomic contributions, as introduced by Hug,[29] attributes this intensity to individual regions of *M*-**2a** and coupling between them. The analysis shows that the intensity is localized predominantly on the alkynyl group (see Figure 10). In addition, there is an important coupling between this group and the helicene ligand, which is not surprising as the helicene generates the strong electronic optical activity of the complex. Other parts of *M*-**2a** clearly do not contribute significantly to the intensity of this mode.
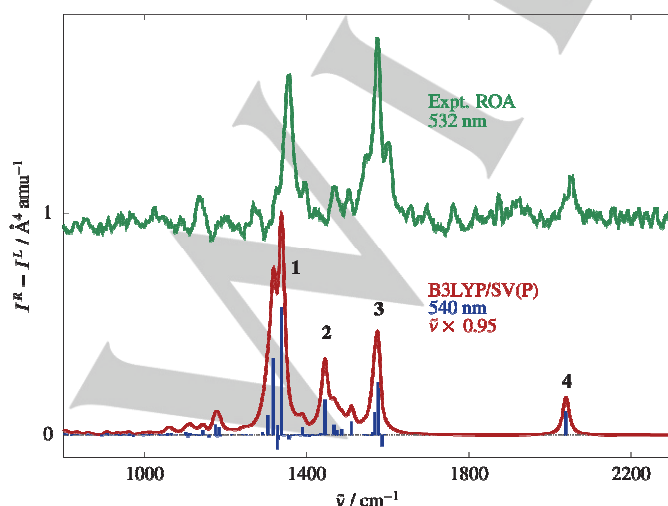

Figure 9. Experimental (top, offset, 532 nm incident wavelength) and calculated (bottom, 540 nm incident wavelength) RROA spectrum for *M*-**2a** (conformer II). The calculated vibrational frequencies were scaled by a factor of 0.95.

A closer inspection reveals that the behavior of the alkynyl stretching mode is largely due to the dependence of the electric dipole-magnetic dipole polarizability *G'* on the molecular structure, in particular the alkynyl bond length, as a function of the incident laser wavelength, as depicted in Figure 11. This plot shows the *xx* element of *G'* as a function of the C≡C bond length for four different incident wavelengths (while *G'* is composed of nine different elements, the *xx* element is chosen here as a representative example). See SI for a full set of data and a full analysis. For the shorter wavelengths G'_{xx} decreases for increasing bond lengths, thus leading to a negative slope. This behavior is reversed for the longer wavelengths, yielding a positive slope. It is exactly this sign change which is responsible for the ROA sign change of the alkynyl stretching mode from negative to positive intensity. It therefore becomes clear that the mono-signate prediction of the simple 2-state model is not straightforwardly transferable to a system like **2a** where the sign of the Raman optical activity of the well-localized alkynyl stretch mode is delicately determined by vibronic coupling with the strongly optically active helicene.
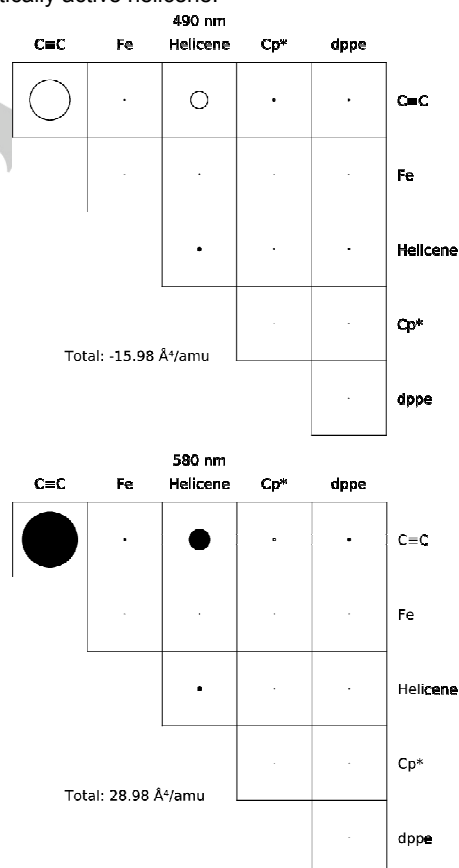

Figure 10. Intensity distribution of the alkynyl stretching mode over different parts of *M*-**2a** for 490 nm (top) and 580 nm (bottom) incident laser wavelength. We adopt the coupling-matrix representation introduced by Hug.[29]
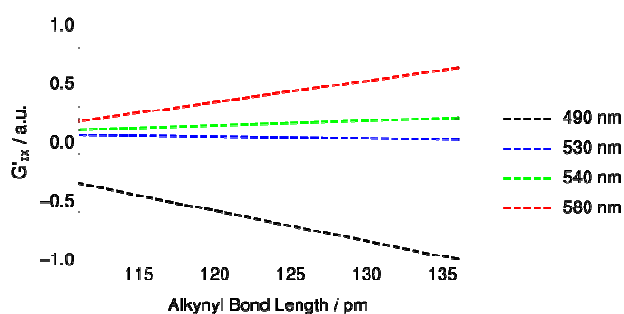
Figure 11. *xx* element of the electric dipole-magnetic dipole polarizability tensor *G'*, as a function of the alkynyl bond length for different wavelengths of the incident laser beam. Note that for each wavelength, *G'* has only been calculate for two bond lengths (111 pm and 136 pm); the dashed lines are not intended to imply a linear relationship but only to help visualizing the trend. Note also that the values of *G'*$_{xx}$ were normalized to the absolute value of the largest element.

Conclusions

In conclusion, new types of organometallic helicene derivatives, consisting of [6]helicenes grafted with one or two iron(II)-ethynyl units, have been prepared and studied, both experimentally and computationally, by a great variety of chiroptical techniques (ECD, OR, VCD and ROA) either in their neutral (**2a**,**b**) or in their cationic oxidized species ([**2a**]$^{•+}$, [**2b**]$^{•+}$ and [**2b**]$^{••2+}$). It was observed that the strong metal-ligand interactions resulted in significant modifications of the chiroptical properties as compared to the starting ligands. Furthermore, the circular dichroism spectra of these novel complexes in the UV-visible and in the near-infrared regions revealed efficient redox-triggered chiroptical switching, showing that the [6]helicene-alkynyl ligand is non-innocent. In the infrared region, the possibility to generate stable radical cations in solution enabled us to examine how the IR and VCD and the Raman and ROA spectra are modified upon oxidation. The strong increase of the dissymmetry factor in the vibrational C≡C stretching mode, with almost two orders of magnitude increase (*g* value up to 0.01) was revealed. Finally, the resonance ROA spectra showed how the graphene-type D and G-modes are slightly tuned upon chemical oxidation using iodine. Accordingly, this technique may be useful for studying other chiral systems such as chiral fullerenes or carbon nanotubes.[15] The calculations confirmed that the observed ROA spectra are consistent with (near-)resonance of the laser and electronic excitations. However, a detailed analysis of the alkynyl stretch ROA signal also indicates that the electronic and vibronic coupling between different moieties in **2a** may create a rather complex behavior as the incident laser wavelength passes through the first ECD band which does not necessarily follow the 2-level model predictions.

Experimental Section

Computational details. Quantum-mechanical structure optimizations, and response calculations performed within RROA studies were carried out at the Kohn-Sham (KS) density functional theory (DFT) level,[30] employing a locally modified version of the NWCHEM program (version

pre-6.8),[10,31] providing complex response tensors.[16c,32-34] Details regarding all the other calculations reported here can be found in the SI. The RROA intensities were calculated according to References [10,16c].A convergence threshold of $1.0 \cdot 10^{-6}$ atomic units (au) was chosen for the iterative solution of the linear response equations. Furthermore, we adopted a value of 0.0173 au for the damping parameter in the complex response calculations, which corresponds roughly to a Gaussian broadening of σ = 0.2 eV matching the width of the electronic circular dichroism (ECD) band of the resonant absorption.[9] A comparison of experimental and simulated ECD spectra for the systems studied (see the SI) showed that most calculated results are deficient, except those obtained with B3LYP.[35] Consequently, this functional was also employed for ROA calculations, together with the def2-SV(P)[36] Gaussian-type basis set. ROA backscattering intensities were calculated by employing the MOVIPAC software suite[37] and its interface with NWCHEM.[10] This setup allows for massively parallel calculations of ROA spectra off, near, or at resonance based on numerical derivatives to evaluate the spectroscopic intensities as first derivates of the respective property tensors. The polarizability derivatives were calculated by adopting a numerical three-point differentiation with respect to Cartesian displacements and a step size of 0.01 au.[38] The dipole-length gauge was chosen in order to allow for computational savings,[39] but we note in passing that the calculation can also be performed with a distributed-origin basis for the magnetic field in order to enforce translational invariance of the spectra.[10] Single-point calculations were considered converged when the total electronic-energy difference between two iteration steps was less than 10^{-10} au. For the structure optimizations, the default values for the maximum and root mean square gradient ($4.5 \cdot 10^{-4}$ au and $3.0 \cdot 10^{-4}$ au) as well as the maximum and root mean square of the Cartesian step ($1.8 \cdot 10^{-3}$ au and $1.2 \cdot 10^{-3}$ au) were employed. The line spectra resulting from this methodology were broadened by means of a convolution with Lorentzian functions featuring a full width at half-maximum (FWHM) of 20 cm^{-1}. For the line broadening, we employed the program MATHEMATICA (version 9.0.1).[40]

Experimental methods. Vibrational circular dichroism (VCD) and infrared (IR) spectra were recorded in a PMA50 optical bench coupled to a Vertex70 spectrometer, both supplied by Bruker©. In the PMA50, the infrared radiation (3800-600 cm^{-1} range) is focused by a BaF$_2$ lens toward a ZnSe photo-elastic modulator (PEM, 50 kHz frequency). The circularly polarized beam is then driven to the sample and finally collected by a D313/QMTC detector. A calibration of the PEM at a fixed wavenumber had been used before recording any VCD spectrum, to ensure a proper chiroptical signal within a spectral region of 600 cm^{-1} around the tuning wavenumber. Typically, calibrations at 1450 cm^{-1} allowed us to obtain a spectrum over the most meaningful region for conjugated organic systems. Every VCD spectrum was the result of averaging a minimum of 36000 scans, recorded at a spectral resolution of 4 cm^{-1}. In order to ensure the absence of linear dichroism interference, caused by preferential orientations within the gels,[41] spectra on different aliquots of these compounds were recorded at different angles without observing appreciable deviations. As a proof of the quality of the recorded data, spectra from pure enantiomeric samples result in mirror images. The samples in dichloromethane at 0.03 M concentration were prepared for vibrational spectra measurements. After thermal treatment, the samples were placed, at room temperature, in a demountable cell A145 (Bruker, Germany) supplied with KBr windows. For the mono-Fe complexes an 0.5 mm Teflon spacer was used to obtain the optimal IR signal for VCD. For the bis-Fe complexes an 0.2 mm Teflon spacer was required at the same concentration.

Raman and Raman optical activity (ROA) spectra were measured using a ChiralRAMAN© spectrometer[42] supplied by BioTools. The samples in dichloromethane at 0.003 M concentration were prepared for ROA measurements. Raman and ROA spectra with a resolution better than 4 cm^{-1} were simultaneously recorded using a quartz cell of 4 mm optical path length. Visible fluorescence from traces of impurities, which can give large backgrounds in Raman spectra, was quenched by leaving the samples to equilibrate in the laser beam before ROA data was acquired.

10

The experimental conditions were as follows: 532 nm laser wavelength, 30 mW laser power at the sample and 12 hours of routine acquisition time. Baseline and flattening procedures were performed to remove the spectral background.

All the remaining experimental methods and procedures can be found either in the SI of this article or in the SI of Ref. [9].

[1]   Selected reviews: a) Y. Shen, C. -F. Chen, *Chem. Rev.* **2012**, *112*, 1463-1535; b) M. Gingras, *Chem. Soc. Rev.* **2013**, *42*, 1051-1095; c) I. G. Stará, I. Starý, in: Siegel, J. S.; Tobe Y. (Eds.), *Science of Synthesis*, vol. 45, Thieme, Stuttgart, **2010**, pp. 885-953; d) A. Rajca, M. Miyasaka, in: T. J. J. Müller, U. H. F. Bunz (Eds.), *Functional Organic Materials* Wiley-VCH, Weinheim, **2007**, pp. 543-577 e) A. Urbano, *Angew. Chem. Int. Ed.* **2003**, *42*, 3986-3989; f) T. J. Katz, *Angew. Chem. Int. Ed.* **2000**, *39*, 1921-1923; g) R. H. Martin, *Angew. Chem. Int. Ed.* **1974**, *13*, 649; h) N. Saleh, C. Shen, J. Crassous, *Chem. Sci.* **2014**, *5*, 3680-3694; i) J. Bosson, J. Gouin, J. Lacour, *Chem. Soc. Rev.* **2014**, *43*, 2824-2840; j) P. Aillard, A. Voituriez, A. Marinetti, *Dalton Trans.* **2014**, *43*, 15263-15278; k) H. Isla, J. Crassous, *C. R. Chimie* **2016**, *19*, 39-49; l) Y. Shen, C.-F. Chen, *Helicenes Chemistry: From Synthesis to Applications*, Springer, Berlin, **2017**.

[2]   a) L. Norel, M. Rudolph, N. Vanthuyne, J. A. G. Williams, C. Lescop, C. Roussel, J. Autschbach, J. Crassous, R. Réau, *Angew. Chem. Int. Ed.* **2010**, *49*, 99-102; b) E. Anger, M. Rudolph, L. Norel, S. Zrig, C. Shen, N. Vanthuyne, L. Toupet, J. A. G. Williams, C. Roussel, J. Autschbach, J. Crassous, R. Réau, *Chem. Eur. J.* **2011**, *17*, 14178-14198; c) E. Anger, M. Rudolph, C. Shen, N. Vanthuyne, L. Toupet, C. Roussel, J. Autschbach, J. Crassous, R. Réau, *J. Am. Chem. Soc.* **2011**, *133*, 3800-3803; d) Shen, C.; Anger, E.; Srebro, M.; Vanthuyne, N.; Toupet, L.; Roussel, C.; Autschbach, J.; Réau, R.; Crassous, J. *Chem. Eur. J.* **2013**, *19*, 16722-1728; e) Crespo, O.; Eguillor, B.; Esteruelas, M. A.; Fernandez, I.; Garcia-Raboso, J.; Gomez-Gallego, M.; Martin-Ortiz, M.; Olivan, M.; Sierra, M. A. *Chem. Comm.* **2012**, *48*, 5328-5330; f) Anger, E.; Srebro, M.; Vanthuyne, N.; Toupet, L.; Rigaut, S.; Roussel, C.; Autschbach, J.; Crassous, J.; Réau, R. *J. Am. Chem. Soc.*, **2012**, *134*, 15628-15631; g) Anger, E.; Srebro, M.; Vanthuyne, N.; Roussel, C.; Toupet, L.; Autschbach, J.; Réau, R.; Crassous, J. *Chem. Comm.* **2014**, *50*, 2854-2856; h) Srebro, M.; Anger, E.; Moore, II, B.; Vanthuyne, N.; Roussel, C.; Réau, R.; Autschbach, J.; Crassous J. *Chem. Eur. J.* **2015**, *21*, 17100-17115; i) C. Shen, X. He, L. Toupet, L. Norel, S. Rigaut, J. Crassous, *Organometallics* **2018**, *37*, 697-705.

[3]   Selected examples: a) J. R. Brandt, X. Wang, Y. Yang, A. J. Campbell and M. J. Fuchter, *J. Am. Chem. Soc.* **2016**, *138*, 9743-9746; b) Y. Yang, B. Rice, X. Shi, J. R. Brandt, R. Correa da Costa, G. J. Hedley, D.-M. Smilgies, J. M. Frost, I. D. W. Samuel, A. Otero-de-la-Roza, E. R. Johnson, K. E. Jelfs, J. Nelson, A. J. Campbell, M. J. Fuchter, *ACS Nano* **2017**, *11*, 8329-8338; c) D. Schweinfurth, M. Zalibera, M. Kathan, C. Shen, M. Mazzolini, N. Trapp, J. Crassous, G. Gescheidt, F. Diederich,. *J. Am. Chem. Soc.* **2014**, *136*, 13045-13052; d) R. A. van Delden, M. K. J. ter Wiel, M. M. Pollard, J. Vicario, N. Koumura, B. L. Feringa, *Nature* **2005**, *437*, 1337-1340; e) T. R. Kelly, H. De Silva, R. A. Silva, *Nature* **1999**, *401*, 150-152; f) T. Verbiest, S. Van Elshocht, M. Kauranen, L. Hellemans, J. Snauwaert, C. Nuckolls, T. J. Katz, A. Persoons, *Science* **1998**, *282*, 913-915.

[4]   Selected reviews: a) F. Paul, C. Lapinte, C. *Coord. Chem. Rev.* **1998**, *178*, 431-509; b) P. J. Low, *Dalton Trans.* **2005**, 2821-2824; c) P. Aguirre-Etcheverry, D. O'Hare, *Chem. Rev.* **2010**, *110*, 4839-4864; d) S. Zalis, R. F. Winter, W. Kaim *Coord. Chem. Rev.* **2010**, 254, 1383-1396; e) G. Grelaud, M. P. Cifuentes, F. Paul, M. G. Humphrey, *J. Organomet. Chem.* **2014**, *751*, 181-200; f) K. Costuas, S. Rigaut, S. *Dalton Trans.* **2011**, *40*, 5643-5658; g) P. A. Schauer, P. J. Low, *Eur. J. Inorg. Chem.* **2012**, 390-411; h) B. J. Coe, *Coord. Chem. Rev.* **2013**, *257*, 1438-1458; i) J. -F. Halet, C. Lapinte, *Coord. Chem. Rev.* **2013**, *257*, 1584-1613.

[5]   Selected examples: a) M. Samoc, N. Gauthier, M. P. Cifuentes, F. Paul, C. Lapinte, M. G. Humphrey, *Angew. Chem. Int. Ed.* **2006**, *45*, 7376-7379; b) M. P. Cifuentes, C. E. Powell, M. G. Humphrey, G. A. Heath, M. Samoc, B. Luther-Davies, *J. Phys. Chem. A* **2001**, *105*, 9625-9627; c) C. E. Powell, M. P. Cifuentes, J. P. Morrall, R. Stranger, M. G. Humphrey, M. Samoc, B. Luther-Davies, G. A. Heath, *J. Am. Chem. Soc.* **2003**, *125*, 602-610; d) K. A. Green, M. P. Cifuentes, T. C. Corkery, M. Samoc, M. G. Humphrey, *Angew. Chem., Int. Ed. Engl.* **2009**, *48*, 7867-7870; e) F. Paul, K. Costuas, I. Ledoux, S. Deveau, J. Zyss, J.-F. Halet, C. Lapinte, *Organometallics* **2002**, *21*, 5229-5235; f) E. Di Piazza, L. Norel, K. Costuas, A. Bourdolle, O. Maury, S. Rigaut, *J. Am. Chem. Soc.* **2011**, 133, 6174-6176; g) K. M. -C. Wong, S. C. -F. Lam, C.-C. Ko, N. Zhu, V. W. -W. Yam, S. Roué, C. Lapinte, S. Fathallah, K. Costuas, S. Kahlal, J.-F. Halet, *Inorg. Chem.* **2003**, *42*, 7086-7097; h) M. Murai, M. Sugimoto, M. Akita, *Dalton Trans.* **2013**, *42*, 16108-16120; i) Y. Liu, C. Lagrost, K. Costuas, N. Tchouar, H. Le Bozec, S. Rigaut, *Chem. Commun.* **2008**, 6117-6119; j) Y. Tanaka, T. Ishisaka, A. Inagaki, T. Koike, C. Lapinte, M. Akita, *Chem. Eur. J.* **2010**, *16*, 4762-4776.

[6]   a) T. Biet, A. Fihey, T. Cauchy, N. Vanthuyne, C. Roussel, J. Crassous, N. Avarvari, *Chem. Eur. J.* **2013**, *19*, 13160-13167; b) J. Nishida, T. Suzuki, M. Ohkita, T. Tsuji, *Angew. Chem. Int. Ed.* **2001**, *40*, 3251-3254; c) Z. Y. Wang, E. K. Todd, X. S. Meng, J. P. Gao, *J. Am. Chem. Soc.* **2005**, *127*, 11552-11553; d) J. K. Zak, M. Miyasaka, S. Rajca, M. Lapkowski, A. Rajca, *J. Am. Chem. Soc.* **2010**, *132*, 3246-3247; e) L. Pospisil, L. Bednarova, P. Stepanek, P. Slavicek, J. Vavra, M. Hromadova, H. Dlouha, J. Tarabek, F. Teply, *J. Am. Chem. Soc.* **2014**, *136*, 10826-10829; f) P. E. Reyes-Gutierrez, M. Jirasek, L. Severa, P. Novotna, D. Koval, P. Sazelova, J. Vavra, A. Meyer, I. Cisarova, D. Saman, R. Pohl, P. Stepanek, P. Slavicek, B. J. Coe, M. Hajek, V. Kasicka, M. Urbanova, F. Teply, *Chem. Comm.* **2015**, *51*, 1583-1586 g) J. R. Brandt, L. Pospısil, L. Bednarova, R. Correa da Costa, A. J. P. White, T. Mori, F. Teply, M. J. Fuchter, *Chem. Commun.* **2017**, *53*, 9059-9062; h) N. Saleh, N. Vanthuyne, J. Bonvoisin, J. Autschbach, M. Srebro-Hooper, J. Crassous, *Chirality* **2018**, doi.org/10.1002/chir.22835.

[7]   Selected examples of VCD of helicenes: a) T. Bürgi, A. Urakawa, B. Behzadi, K.-H. Ernst, A. Baiker, *New. J. Chem.* **2004**, *28*, 332-334; b) S. Abbate, G. Longhi, F. Lebon, F. Fontana, T. Caronna, D. A. Lightner, *Phys. Chem. Chem. Phys.* **2009**, *11*, 9039-9043; c) S. Abbate, G. Longhi, F. Lebon, E. Castiglioni, S. Superchi, L. Pisani, F. Fontana, F. Torricelli, T. Caronna, R. Villani, R. Sabia, M. Tommasini, A. Lucotti, D.; Mendola, A. Mele, D. A. Lightner, *J. Phys. Chem. C* **2014**, *118*, 1682-1695; d) A. H. Pandith, N. Islam, Z. F. Syed, S. -u Rehman, S. Bandaru, A. Anoop, *Chem. Phys. Lett.* **2011**, *516*, 199-203; e) T. B. Freedman, X. Cao, A; Rajca, H. Wang, L. A. Nafie, *J. Phys. Chem. A* **2003**, *107*, 7692-7696; f) C. Herse, D. Bas, F. C. Krebs, T. Bürgi, J. Weber, T. Wesolowski, B. W. Laursen, J. Lacour, *Angew. Chem. Int. Ed.* **2003**, *42*, 3162-3166; g) P. Mobian, C. Nicolas, E. Francotte, T. Bürgi, J. Lacour, *J. Am. Chem. Soc.* **2008**, *130*, 6507-6514; h) F. Torricelli, J. Bosson, C. Besnard, M. Chekini, T. Bürgi, J. Lacour, *Angew. Chem. Int. Ed.* **2013**, *52*, 1796-1800; i) V. P. Nicu, J.

11

Neugebauer, S. K. Wolff, E. J. Baerends, *Theor. Chem. Account* **2008**, *119*, 245-263; j) V. Liégeois, B. Champagne, *J. Comput. Chem.* **2009**, 30, 1261-1278.

[8] Experimental ROA of helicenes: a) C. Johannessen, E. W. Blanch, C. Villani, S. Abbate, G. Longhi, N. R. Agarwal, M. Tommasini, D. A. Lightner, *J. Phys. Chem. B* **2013**, *117*, 2221-2230. Theoretical ROA of helicenes: b) V. Liegeois, B. Champagne, *Theor. Chem. Acc.* **2012**, *131*, 1284; c) M. Tommasini, G. Longhi, G. Mazzeo, S. Abbate, B. Nieto-Ortega, F. J. Ramírez, J. Casado, J. T. L. Navarrete, *J. Chem. Theory Comput.* **2014**, *10*, 5520-5527; d) V. Liégeois, B. Champagne, *J. Comput. Chem.* **2009**, *30*, 1261-1278.

[9] C. Shen, G. Loas, M. Srebro-Hooper, N. Vanthuyne, L. Toupet, O. Cador, F. Paul, J. T. López Navarrete, F. J. Ramírez, B. Nieto-Ortega, J. Casado, J. Autschbach, M. Vallet, J. Crassous, *Angew. Chem. Int. Ed.* **2016**, *55*, 8062-8066.

[10] F. Krausbeck, J. Autschbach, M. Reiher, *J. Phys. Chem. A* **2016**, *120*, 9740-9748.

[11] a) R. Denis, L. Toupet, F. Paul, C. Lapinte, *Organometallics* **2000**, *19*, 4240-421; b) F. Paul, J. -Y. Mevellec, C. Lapinte, *Dalton Trans.* **2002**, 1783-1790; c) F. Paul, G. da Costa, A. Bondon, N. Gauthier, S. Sinbandhit, L. Toupet, K. Costuas, J. -F. Halet, C. Lapinte, *Organometallics* **2007**, *26*, 874-896; d) F. Paul, A. Bondon, G. da Costa, F. Malvolti, S. Sinbandhit, O. Cador, K. Costuas, L. Toupet, M.-L. Boillot, *Inorg. Chem.* **2009**, *48*, 10608-10624; e) C. Roger, P. Hamon, L. Toupet, H. Rabaa, J.- Y. Saillard, J. -R. Hamon, C. Lapinte, *Organometallics* **1991**, *10*, 1045-1054; f) F. Paul, L. Toupet, J.-Y. Thépot, K. Costuas, J.-F Halet, C. Lapinte, *Organometallics* **2005**, *24*, 5464-5478.

[12] a) J. Autschbach, *Chirality* **2009**, *21*, E116-E152; b) J. Autschbach, L. Nitsch-Velasquez, M. Rudolph, *Top. Curr. Chem.* **2011**, *298*, 1-98; c) M. Srebro-Hooper, J. Autschbach, *Annu. Rev. Phys. Chem.* **2017**, *68*, 399-420.

[13] a) L. D. Barron, *Molecular Light Scattering and Optical Activity* 2nd Edition, Cambridge, **2009**; b) L. A. Nafie, *Vibrational Optical Activity: Principles and Applications*, Wiley, **2010**; c) P. L. Polavarapu, *Chiroptical Spectroscopy: Fundamentals and Applications*, CRC Press, **2016**.

[14] a) Y. He, X. Cao, L. A. Nafie, T. B. Freedman, *J. Am. Chem. Soc.* **2001**, *123*, 11320-11321; b) S. R. Domingos, A. Huerta-Viga, L. Baij, S. Amirjalayer, D. A. E. Dunnebier, A. J. C. Walters, M. Finger, L. A. Nafie, B.; de Bruin, W. J. Buma, S. Woutersen, *J. Am. Chem. Soc.* **2014**, *136*, 3530-3535 and references therein.

[15] a) E. Di Donato, M. Tommasini, G. Fustella, L. Brambilla, C. Castiglioni, G. Zerbi, C. D. Simpson, K. Mullen, F. Negri, *Chem. Phys.* **2004**, *301*, 81-93; b) C. Castiglioni, M. Tommasini, G. Zerbi, *Philos. Trans. R. Soc., A* **2004**, *362*, 2425-2459; c) M. Tommasini, C. Castiglioni, G. Zerbi, *Phys. Chem. Chem. Phys.*, **2009**, *11*, 10185-10194.

[16] a) L. A. Nafie, *Chem. Phys.* **1996**, *205*, 309-322; c) M. Vargek, T. B. Freedman, E. Lee, L. A. Nafie, *Chem. Phys. Lett.* **1998**, *287*, 359-364; c) L. Jensen, J. Autschbach, M. Krykunov, G. C. Schatz, *J. Chem. Phys.* **2007**, *127*, 134101; d) S. Luber, J. Neugebauer, M. Reiher, *J. Chem.*

Phys. **2010**, *132*, 044113; e) C. Merten, H. Li, L. A. Nafie, *J. Phys. Chem. A* **2012**, *116*, 7329-7336; f) M. Magg, Y. Kadria-Vili, P. Oulevey, R. B. Weisman, T. Bürgi, *J. Phys. Chem. Lett.* **2016**, *7*, 221-225.

[17] L. D. Barron, D. A. Long, *J. Raman Spectrosc.* **1983**, *14*, 219-219.

[18] L. D. Barron, L. Hecht, I. H. McColl, E. W. Blanch, *Mol. Phys.* **2004**, *102*, 731-744.

[19] L. D. Barron, M. P. Bogaard, A. D. Buckingham, *J. Am. Chem. Soc.* **1973**, *95*, 603-605.

[20] C. Herrmann, M. Reiher, *Top. Curr. Chem.* **2007**, *268*, 85-132.

[21] E. W. Blanch, L. Hecht, L. D. Barron, *Protein Sci.* **1999**, *8*, 1362-1367.

[22] A. N.; Batista, J. M. Batista, Jr., V. S. Bolzani, M. Furlan, E. W. Blanch, *Phys. Chem. Chem. Phys.* **2013**, *15*, 20147-20152.

[23] N. Berova, P. Polavarapu, K. Nakanishi, R. Woody, *Advances in Chiroptical Methods*; Wiley Blackwell: New York, **2011**.

[24] J. Haesler, I. Schindelholz, E. Riguet, C. G. Bochet, W. Hug, *Nature* **2007**, *446*, 526-529.

[25] J. Sebestik, P. Bour, *J. Phys. Chem. Lett.* **2011**, *2*, 498-502.

[26] M. Reiher, V. Liégeois, K. Ruud, *J. Phys. Chem. A* **2005**, *109*, 7567-7574.

[27] J. Costante, L. Hecht, P. L. Polavarapu, A. Collet, L. D. Barron, *Angew. Chem. Int. Ed.* **1997**, *36*, 885-887.

[28] L. N. Vidal, T. Giovannini, C. Cappelli, *J. Phys. Chem. Lett.* **2016**, *7*, 3585-3590.

[29] W. Hug, *Chem. Phys.* **2001**, *264*, 53-69.

[30] R. G. Parr, Density functional theory of atoms and molecules. In Horizons of Quantum Chemistry; Springer: 1980 pages 5–15.

[31] M. Valiev, E. Bylaska, N. Govind, K. Kowalski, T. Straatsma, H. V. Dam, D. Wang, J. Nieplocha, E. Apra, T. Windus, W. de Jong, *Comput. Phys. Commun.* **2010**, *181*, 1477-1489.

[32] J. Autschbach, *Comp. Lett.* **2007**, *3*, 131-150.

[33] M. Krykunov, J. Autschbach, *J. Chem. Phys.* **2005**, *123*, 114103.

[34] J. Autschbach, *ChemPhysChem* **2011**, *12*, 3224-3235.

[35] a) A. D. Becke, *J. Chem. Phys.* **1993**, *98*, 5648-5652; b) C. Lee, W. Yang, R. G. Parr, *Phys. Rev. B* **1988**, *37*, 785-789; c) S. H. Vosko,, L. Wilk, M. Nusair, *Can. J. Phys.* **1980**, *58*, 1200-1211; d) P. Stephens, F. Devlin, C. Chabalowski, M. J. Frisch, *J. Phys. Chem.* **1994**, *98*, 11623-11627.

[36] A. Schäfer, H. Horn, R. Ahlrichs, *J. Chem. Phys.* **1992**, *97*, 2571-2577.

[37] T. Weymuth, M. P. Haag, K. Kiewisch, S. Luber, S. Schenk, C. R. Jacob, C. Herrmann, J. Neugebauer, M. Reiher, *J. Comput. Chem.* **2012**, *33*, 2186-2198.

[38] M. Reiher, J. Neugebauer, B. A. Hess, *Z. Phys. Chem.* **2003**, *217*, 91-103.

[39] I. Grant, *J. Phys. B: Atomic and Molecular Physics* **1974**, *7*, 1458.

[40] Wolfram Research, "Mathematica 9.0.1", 2013.

[41] A. Brizard, D. Berthier, C. Aimé, T. Buffeteau, D. Cavagnat, L. Ducasse, I. Huc, R. Oda, *Chirality* **2009**, *21*, S153-S162.

[42] W. Hug, G. Hangartner, *J. Raman Spectrosc.* **1999**, *30*, 841-852.

12

Entry for the Table of Contents

FULL PAPER

Chiroptical properties (ECD, VCD, RROA) and redox-switching activity of iron-alkynyl-helicenes are studied exprimentally and theoretically.

Redox chiropical switch

ECD

VCD RROA

Red ⇌ Ox

Experiment / theory
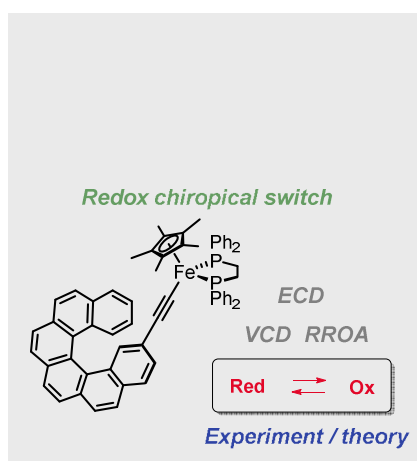
Chengshuo Shen, Monika Srebro-Hooper, Thomas Weymuth, Florian Krausbeck, Juan T. López Navarrete, Francisco J. Ramírez, Belén Nieto-Ortega, Juan Casado, Markus Reiher, Jochen Autschbach,* and Jeanne Crassous*

Page No. – Page No.

Redox-active Chiroptical Switching in Mono- and Bis-Iron-Ethynyl-Carbo[6]Helicenes Studied by Electronic and Vibrational Circular Dichroism and Resonance Raman Optical Activity